Research article

Giuseppe Castaldi, Victor Pacheco-Peña, Massimo Moccia, Nader Engheta* and Vincenzo Galdi*

Exploiting space-time duality in the synthesis of impedance transformers via temporal metamaterials

https://doi.org/10.1515/nanoph-2021-0231
Received May 11, 2021; accepted July 22, 2021;
published online August 18, 2021

Abstract: Multisection quarter-wave impedance transformers are widely applied in microwave engineering and optics to attain impedance-matching networks and antireflection coatings. These structures are mostly designed in the spatial domain (time harmonic) by using geometries of different materials. Here, we exploit such concepts in the time domain by using time-varying metamaterials. We derive a formal analogy between the spectral responses of these structures and their temporal analogs, i.e., time-varying stepped refractive-index profiles. We show that such space-time duality grants access to the vast arsenal of synthesis approaches available in microwave engineering and optics. This allows, for instance, the synthesis of temporal impedance transformers for broadband impedance matching with maximally flat or equi-ripple responses, which extend and generalize the recently proposed quarter-wave design as an antireflection temporal coating. Our results, validated via full-wave numerical simulations, provide new insights and deeper understanding of the wave dynamics in time-varying media, and may find important applications in space-time metastructures for broadband frequency conversion and analog signal processing.

Keywords: broadband; frequency conversion; impedance matching; metamaterials; time-varying.

1 Introduction

The study of wave interactions with time-varying media and structures is a subject of a longstanding interest in electromagnetics [1–3], which has recently gained new momentum in the emerging field of space-time metamaterials and metasurfaces [4–7]. In these artificial materials, the conventional *spatial* modulation of the constitutive parameters is synergistically coupled with *temporal* modulation, thereby enabling a wealth of intriguing field-manipulation effects and anomalous wave-matter interactions. These include, for instance, magnetless nonreciprocity [8–14], time reversal and holography [15], extreme energy accumulation [16], Doppler effect [17], inverse prism [18], Fresnel drag [19], harmonic beam steering and shaping [20–22], temporal [23] and spatiotemporal diffraction gratings [24], broadband impedance matching [25, 26] and absorption [27], time-varying optical vortices [28], temporal aiming [29], Brewster angle [30], spatiotemporal isotropic-to-anisotropic meta-atoms [31], parity-time symmetry [32], and exceptional points [33], among others.

Interestingly, recent theoretical studies have shown how the space-time duality can be leveraged to extend to the realm of time-varying metastructures some concepts and tools conventionally utilized in spatially variant scenarios. For instance, the reflection and transmission of electromagnetic waves at temporal boundaries [1, 3, 34] were studied in terms of temporal Fresnel coefficients, highlighting the wavenumber conservation and frequency conversion. The case of "temporal slabs" was also studied [35], and theoretical formalisms based on the transfer-matrix

***Corresponding authors: Nader Engheta**, Department of Electrical and Systems Engineering, University of Pennsylvania, Philadelphia, PA, 19104, USA, E-mail: engheta@seas.upenn.edu. https://orcid.org/0000-0003-3219-9520; and **Vincenzo Galdi**, Fields & Waves Lab, Department of Engineering, University of Sannio, Benevento, I-82100, Italy, E-mail: vgaldi@unisannio.it. https://orcid.org/0000-0002-4796-3600
Giuseppe Castaldi and Massimo Moccia, Fields & Waves Lab, Department of Engineering, University of Sannio, Benevento, I-82100, Italy, E-mail: castaldi@unisannio.it (G. Castaldi), massimo.moccia@unisannio.it (M. Moccia). https://orcid.org/0000-0003-4400-9990 (G. Castaldi). https://orcid.org/0000-0003-3614-2871 (M. Moccia)
Victor Pacheco-Peña, School of Mathematics, Statistics and Physics, Newcastle University, Newcastle Upon Tyne, NE1 7RU, UK, E-mail: Victor.Pacheco-Pena@newcastle.ac.uk. https://orcid.org/0000-0003-2373-7796

[36], effective-medium theory [37], and higher-order homogenization schemes [38] were proposed to model "temporal multilayers" or "temporal multisteps". These scenarios can be considered as the temporal equivalent of spatial multi-layered media [39] with the difference that in the former case time-varying media with stepped permittivity profiles are implemented for the whole spatially unbounded medium where the wave travels. Within this framework, by translating to the temporal case the well-known quarter-wave impedance-matching scheme in microwave engineering [40], the idea of antireflection temporal coatings [41] was also put forward in order to attain reflectionless frequency conversion and to achieve impedance matching in spatiotemporal scenarios. More recently, this idea was further expanded to more general temporal multisteps in order to attain higher-order transfer functions [42], and several design examples inspired by spatial-multilayer counterparts were discussed. However, the systematic synthesis of the desired transfer function remains an open problem.

Here, we exploit the space-time duality that exists between spatial and temporal boundaries to introduce a rigorous and systematic framework for the synthesis of temporal media having temporal multistep permittivity functions. First, we prove analytically that, under carefully engineered conditions, there exists a remarkably simple, and yet nonintuitive, mathematical relationship that connects the reflectivity of a temporal multistep and the insertion loss of a conventional spatial multilayer. This result bears important practical implications since it enables the direct exploitation of the vast arsenal of synthesis approaches that have been developed in microwave engineering for the design of spatial quarter-wave multilayered impedance transformers [40]. As a proof of concept, here we show that the general synthesis approach developed by Riblet in the 1950s [43] for the spatial case can be seamlessly applied to the synthesis of broadband temporal impedance-matching transformers. As it will be shown, for a temporal boundary between lossless dielectrics, this approach allows the synthesis of arbitrary, real-valued polynomial transfer functions by resorting to temporal sections featuring real-valued positive refractive indices.

Accordingly, the rest of the manuscript is structured as follows. In Section 2, we outline the problem formulation, highlight the formal analogies between the responses of spatial and temporal multisteps, and illustrate the synthesis approach. In Section 3, we demonstrate some representative syntheses featuring maximally flat (binomial) and equi-ripple (Chebyshev) responses. Moreover, we validate the approach by comparison with full-wave numerical simulations in the presence of narrowband and broadband input signals, and for unbounded and bounded regions. Finally, in Section 4, we provide some brief conclusions and discuss possible perspectives. Some ancillary details on the analytical and computational aspects are provided in Section 5. Our results, which include the temporal quarter-wave design [41] as a special case, provide new insights and deeper understanding of the role and possible applications of temporal boundaries by exploiting the space-time duality in the study of wave propagation in temporal metamaterials and pave the way to novel exciting developments in this emerging field.

2 Analytical formulation and results

2.1 Spatial multilayered impedance transformers

Referring to Figure 1(A) for schematic illustration, we start considering a simple configuration of a spatial impedance transformer, featuring a multilayered structure made of M dielectric layers (with refractive index n_m and thickness d_m, $m = 1, \ldots, M$) stacked along the x-direction and sandwiched between semi-infinite regions with refractive index n_i (input, $x < 0$) and n_e (exterior, $x > x_M = d_1 + d_2 + \cdots + d_M$). Throughout this study, we assume a time-harmonic $\exp(-i\omega t)$ time-dependence, and nonmagnetic, lossless media (i.e., real-valued refractive indices). Moreover, we assume that the operating frequencies are much smaller than any material resonance frequencies. In so doing, the materials can approximately be considered as being nondispersive [1, 29, 41, 42, 44]. As detailed in the Methods Section 5.1, for normally incident plane-wave illumination, the field propagation inside the multilayer can be rigorously described via the transfer-matrix formalism [39], with the (dimensionless, unimodular) matrix

$$\underline{\underline{S}}_m(\theta) = \begin{bmatrix} \cos\theta & \dfrac{i}{v_m}\sin\theta \\ i v_m \sin\theta & \cos\theta \end{bmatrix} \tag{1}$$

relating the transverse electric and magnetic field components (suitably normalized) at the two interfaces of the generic mth layer. In Equation (1), $v_m = n_m/n_i$ indicates the normalized refractive index (with respect to that of the input section), and $\theta = k n_m d_m$ the electrical thickness, which we assume is identical for all layers; here, $k = \omega/c = 2\pi/\lambda$ denotes the wavenumber in a vacuum, and c and λ the

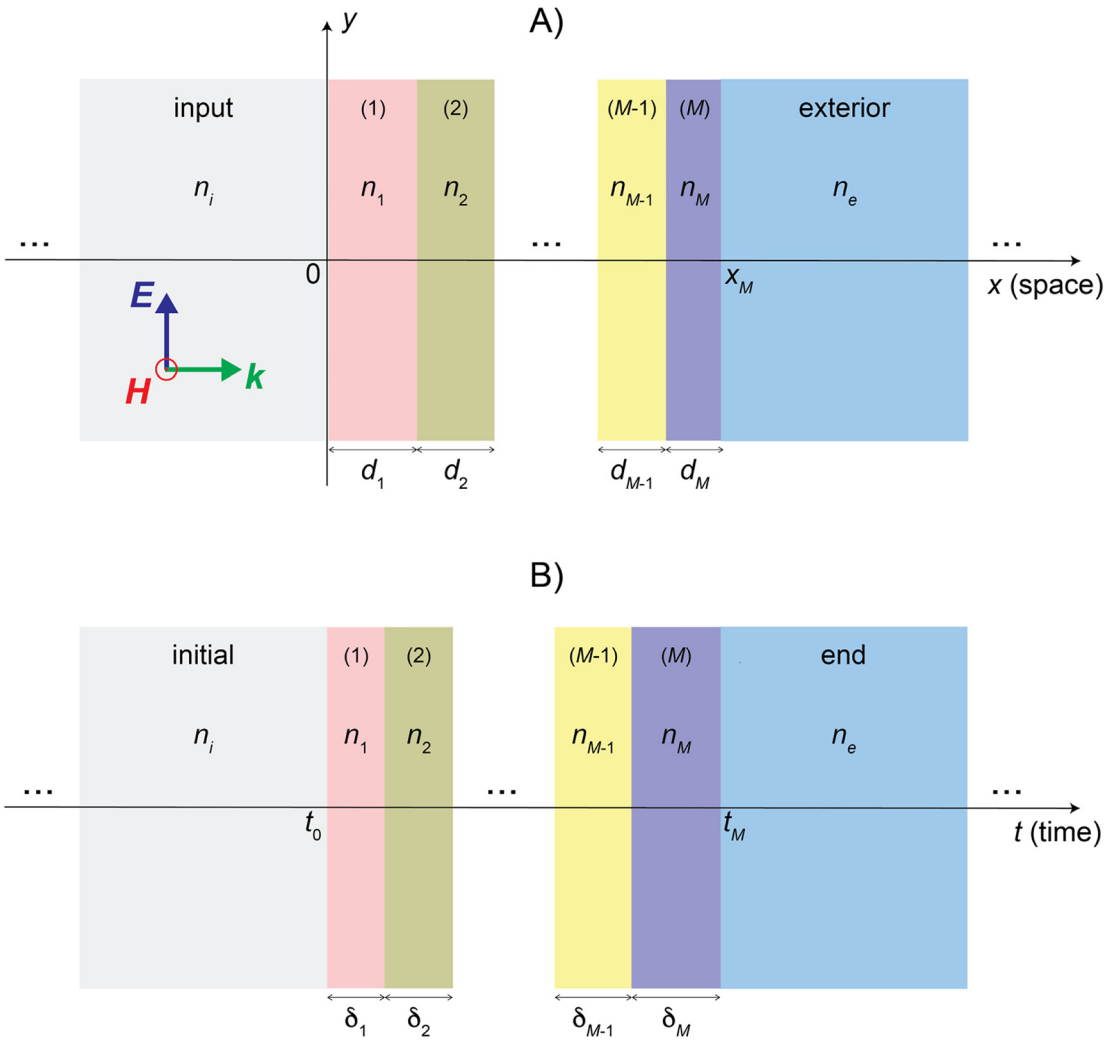

Figure 1: Problem schematic.
(A) Spatial multilayer (with refractive indices n_m and thicknesses d_m, $n = 1, \ldots, M$) sandwiched between two semi-infinite regions with refractive indices n_i (input) and n_e (exterior), under normally incident, plane-wave illumination. (B) Temporal transition (in a spatially unbounded medium) of the refractive index between the values n_i (initial) and n_e (end) via a multistep profile (temporal multistep, with refractive indices n_m and durations δ_m, $n = 1, \ldots, M$).

corresponding speed of light and wavelength, respectively. By chain multiplication, we can straightforwardly relate the transverse fields at the input ($x = 0$) and output ($x = x_M$) interfaces via the total transfer matrix [39]

$$\underline{\underline{S}} = \prod_{m=M}^{1} \underline{\underline{S}}_m = \begin{bmatrix} s_{11} & is_{12} \\ is_{21} & s_{22} \end{bmatrix}, \tag{2}$$

where s_{11}, s_{12}, s_{21}, and s_{22} are real-valued and satisfy the (unimodular) condition $s_{11}s_{22} + s_{12}s_{21} = 1$. From there, the reflection coefficient can be obtained as (see the Methods Section 5.1 for further details)

$$\rho = \frac{s_{22} + is_{21} - v_e(s_{11} + is_{12})}{s_{22} - is_{21} + v_e(s_{11} - is_{12})}, \tag{3}$$

with $v_e = n_e/n_i$. In a typical impedance-matching scenario, for a given index mismatch between the input and exterior regions, the general problem entails synthesizing the multilayer in such a way that reflections are minimized over a broad frequency range [40]. Within this framework, for moderately small index mismatches, the *small-reflection* approximation (which essentially neglects multiple reflections inside the multilayer) provides a very simple and effective parameterization that enables systematic Fourier-based synthesis strategies [40]. However, such approximation does not provide any major advantage when applied to the temporal counterpart of interest in this study and therefore is not pursued here.

2.2 Temporal multistep impedance transformers

Let us now consider the temporal counterpart schematically illustrated in Figure 1(B). As in Section 2.1, here we again start considering a monochromatic electromagnetic wave as the incident signal. In the temporal case, however, this wave travels within a homogeneous and spatially unbounded medium having an initial refractive index n_i for times $t < t_0$. Starting at a time instant $t = t_0$, we assume a temporal modulation of the refractive index characterized by M intervals (each of duration δ_m, featuring an ideal step transition to a refractive index n_m), reaching an end value n_e at time $t_M = \delta_1 + \delta_2 + \cdots + \delta_M$. Specifically, we only consider changes of the refractive index produced by nonmagnetic media with time-varying permittivity. Clearly, the assumption of step temporal transitions is highly idealized, as it implies that the medium response to modulation is infinitely fast. In reality, a rise/fall time should be considered when changing the permittivity of the medium. In this context, as long as such fall/rise time is much smaller than the period of the incident wave, our approach will continue to be valid. Indeed, in our numerical simulations (see the Methods Section 5.3) we do assume fast but still smooth transitions with short rise/fall times, in order to obtain accurate results and for the simulator to converge.

Note that, in order to better highlight the formal analogies with the spatial scenario, we have utilized the same symbols M, n_i, n_e, and n_m, although their physical meaning is now evidently different. As detailed in the Methods Section 5.1, also for this temporal multistep, it is possible to study the wave propagation via a rigorous transfer-matrix approach. Specifically, by suitably normalizing the relevant electric and magnetic induction fields, we can obtain a transfer matrix formally analogous to that in Equation (1), viz. [37],

$$\underline{\underline{S}}_m(\varphi) = \begin{bmatrix} \cos\varphi & \dfrac{i}{\nu_m}\sin\varphi \\ i\nu_m \sin\varphi & \cos\varphi \end{bmatrix}, \tag{4}$$

with $\varphi = \omega\delta_m/\nu_m$ now denoting the normalized travel time, once again assumed identical for all intervals. Accordingly, by chain multiplication, we can obtain the transfer matrix connecting the (normalized) electric and magnetic induction fields at the initial ($t = t_0$) and final ($t = t_M$) temporal boundaries, which is formally identical to the expression in Equation (2) (but with argument φ instead of θ). From there, the backward (BW) wave coefficient, which is the temporal analog of the reflection coefficient, can be derived as (see the Methods Section 5.1 for more details)

$$R = \frac{s_{22} + is_{21}}{2\nu_e^2} - \frac{s_{11} + is_{12}}{2\nu_e}. \tag{5}$$

We highlight that, in spite of the aforementioned formal analogies, the above expression differs from that in Equation (3) since, in view of causality, the reflection coefficient assumes different meanings in the spatial and temporal cases. Nevertheless, as discussed hereafter, the space-time duality can be directly exploited by resorting to different observables.

2.3 Formal analogies

In microwave engineering, rigorous approaches to the synthesis of spatial multilayered impedance transformers typically consider as a meaningful parameter the *insertion loss* (or power loss ratio) [40]

$$P_L = \frac{1}{1-|\rho|^2} = \frac{1}{2} + \frac{\nu_e\left(s_{11}^2 + s_{12}^2\right)}{4} + \frac{s_{22}^2 + s_{21}^2}{4\nu_e}, \tag{6}$$

where the second equality follows from Equation (3) taking into account the unimodular condition. On the other hand, from Equation (5) and similar arguments, we obtain for the temporal case

$$|R|^2 = \nu_e^{-3}\left[-\frac{1}{2} + \frac{\nu_e\left(s_{11}^2 + s_{12}^2\right)}{4} + \frac{s_{22}^2 + s_{21}^2}{4\nu_e}\right], \tag{7}$$

from which the formal analogy with the insertion loss in Equation (6) becomes apparent. Specifically, by suitably mapping the arguments ($\theta \leftrightarrow \varphi$, i.e., $kn_m d_m \leftrightarrow \omega\delta_m/\nu_m$), we obtain

$$P_L - 1 = \nu_e^3 |R|^2, \tag{8}$$

which represents the key result in our study, and the cornerstone of our proposed synthesis approach. We stress that, in spite of its remarkably simple form, this result is neither trivial nor intuitive, as it connects two different observables (spatial insertion loss and temporal reflectivity). By recalling the well-known expressions for the spatial reflection coefficient [39] and temporal BW coefficient [34] in the absence of the multilayer and multistep, respectively (i.e., $\theta = \varphi = 0$, corresponding to a single spatial/temporal boundary between media with refractive indices n_i and n_e),

$$\rho(0) = \frac{n_i - n_e}{n_i + n_e} = \frac{1-\nu_e}{1+\nu_e}, \tag{9}$$

$$R(0) = \frac{n_i(n_i - n_e)}{2n_e^2} = \frac{1-\nu_e}{2\nu_e^2}, \tag{10}$$

it can be readily verified that Equation (8) consistently holds in this especially simple case. However, our theory

ensures that this result also holds in the presence of *generic* spatial and temporal multisteps, under the argument mapping $\theta \leftrightarrow \varphi$.

In what follows, we show how this formal analogy can be leveraged to exploit the wealth of synthesis tools and approaches developed in microwave engineering for impedance transformers using time-varying media.

2.4 Synthesis strategy

As described in the introduction, a well-known synthesis approach for broadband spatial quarter-wave multilayered impedance transformers is based on a theory put forward by Riblet in the 1950s [43], which systematizes and generalizes some previous results by Collin [45]. This approach allows the physically feasible synthesis of insertion-loss functions belonging to the general family

$$P_L(\theta) = 1 + Q_M^2(\cos\theta), \tag{11}$$

where Q_M is a real-valued, Mth degree polynomial. When particularized to our spatial multilayered scenario in Figure 1(A), the above theory prescribes spatial quarter-wave thickness for the layers

$$n_m d_m = \frac{\lambda_0}{4}, \quad m = 1, \ldots, M, \tag{12}$$

with $\lambda_0 = 2\pi c/\omega_0$ denoting the vacuum wavelength at the desired center angular frequency ω_0. Moreover, for n_i and n_e real and positive, it guarantees that the resulting refractive indices n_m of the M layers are likewise real and positive, and provides a constructive procedure for their calculation; for the sake of completeness, the salient steps of the approach are summarized in the Methods Section 5.2.

In view of the formal analogy in Equation (8), the same approach enables the rigorous, systematic synthesis of temporal multisteps (as in Figure 1(B)) with rather general reflectivity functions of polynomial type,

$$|R(\varphi)|^2 = \nu_e^{-3} Q_M^2(\cos\varphi), \tag{13}$$

by exploiting *the same* (real, positive) refractive indices as for the spatial case above. In this case, the travel times of the steps are chosen as

$$\frac{\delta_m}{\nu_m} = \frac{T_0}{4}, \quad m = 1, \ldots, M, \tag{14}$$

with $T_0 = 2\pi/\omega_0$ denoting the period (in vacuum) at the desired center frequency. We note that, in both spatial and temporal cases, the polynomial function Q_M must satisfy the self-consistency relationship (in the limit $\theta, \varphi \to 0$, i.e., in the absence of the multilayer/multistep)

$$Q_M^2(1) = P_L(0) - 1 = \nu_e^3 |R(0)|^2 = \frac{(1-\nu_e)^2}{4\nu_e}. \tag{15}$$

In what follows, we focus on two traditional designs known for broadband spatial antireflection coatings, namely, the *maximally flat* and *equi-ripple* responses, which we then implement with temporal metamaterials to achieve their temporal analog. Interestingly, for these designs, it can be shown [43] that the (normalized) refractive indices also satisfy the symmetry conditions

$$\nu_m \nu_{M+1-m} = \nu_e, \quad m = 1, \ldots, M. \tag{16}$$

We note that, for the special case $M = 1$, the result in Equation (16) consistently reproduces the quarter-wave design $n_1 = \sqrt{n_i n_e}$ that was previously extended to the temporal case [41].

3 Broadband temporal impedance transformers

3.1 Spatially unbounded medium

We start considering the spatially unbounded-medium scenario in Figure 1(B), assuming as initial and end values for the refractive indices $n_i = 1$ and $n_e = 2$, respectively, and $M = 4$ intervals.

As a first synthesis example, we consider the so-called *binomial* design [40],

$$|R(\varphi)| = \frac{|1-\nu_e|}{2\nu_e^2} |\cos\varphi|^M, \tag{17}$$

which ensures a maximally flat frequency response. Note that the multiplicative constant in Equation (17) is selected so as to fulfill the self-consistency condition in Equation (10).

By applying the previously described synthesis strategy, we obtain for the four temporal intervals: $n_1 = 1.044$, $n_2 = 1.242$, $n_3 = 1.610$, and $n_4 = 1.915$ [which satisfy the symmetry conditions in Equation (16)], with the corresponding durations obtained via Equation (14): $\delta_1 = 0.261T_0$, $\delta_2 = 0.311T_0$, $\delta_3 = 0.403T_0$, and $\delta_4 = 0.479T_0$.

Figure 2 shows some representative results for this design. Specifically, Figure 2(A) shows a finite-element computed (see Section 5.3 for details) space-time field map pertaining to a *narrowband* modulated (~12 cycle) Gaussian pulse with center angular frequency chosen as the design value ω_0, from which we observe the expected frequency conversion [1, 3] in the forward (FW) propagating waves at the temporal boundaries, but without visible BW reflected components, as an effect of the

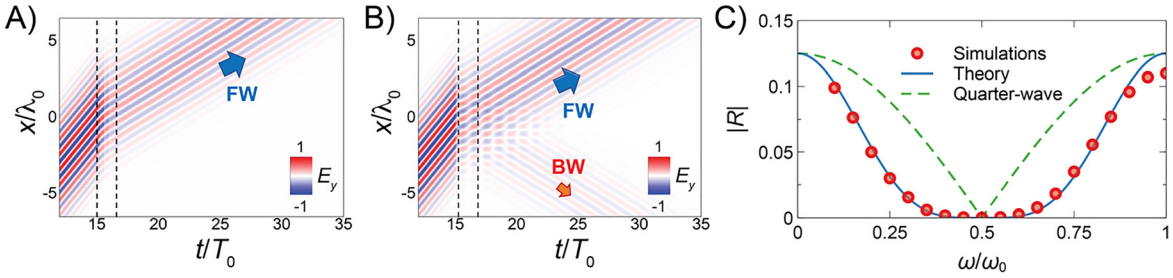

Figure 2: Binomial design: $n_i = 1$, $n_e = 2$, $M = 4$, $n_1 = 1.044$, $n_2 = 1.242$, $n_3 = 1.610$, $n_4 = 1.915$, $\delta_1 = 0.261T_0$, $\delta_2 = 0.311T_0$, $\delta_3 = 0.403T_0$, and $\delta_4 = 0.479T_0$.
(A), (B) Numerically computed space-time maps (normalized electric field) for narrowband modulated Gaussian pulses with center angular frequency ω_0 and $0.2\omega_0$, respectively. The vertical dashed lines indicate the initial ($t_0 = 15T_0$) and final ($t_M = 16.453T_0$) temporal boundaries. (C) Comparison between numerically computed (red circles) and theoretical (blue-solid curve) BW wave coefficient magnitude as a function of normalized angular frequency (in the final medium). Also shown (green-dashed curve), as a reference, is the response of the quarter-wave design ($M = 1$, $n_1 = 1.414$, and $\delta_1 = 0.354T_0$).

impedance matching. As shown in Figure 2(B), these BW waves become clearly visible if the center angular frequency of the pulse differ substantially ($0.2\omega_0$) from the design value, thereby indicating that the impedance matching is less effective. For a more quantitative assessment, we carry out multiple numerical simulations by varying the center frequency of the narrowband pulse, so as to cover the spectral range of interest, and estimate the BW wave coefficient from the amplitude of the BW component (normalized by the incident one). As shown in Figure 2(C), these results are in excellent agreement with the theoretical design in Equation (17), yielding the desired maximally flat behavior; note that the response is centered at $\omega_0/2$ in view of the frequency conversion ($\omega_e = n_i\omega_i/n_e$) imparted by the final temporal boundary (with $n_e = 2$). We also observe the expected broader bandwidth by comparison with the reference quarter-wave design (i.e., $M = 1$) that was previously studied [41]. Within this framework, paralleling the spatial case [40], it is rather straightforward to estimate analytically the bilateral fractional bandwidth for a given maximum tolerable BW wave coefficient $R_{\max} = |R(\varphi_{\max})|$, viz.,

$$\frac{\Delta\omega}{\omega_0} = 2 - \frac{4\varphi_{\max}}{\pi}, \tag{18}$$

where $\varphi_{\max}$ follows by inverting Equation (17) as

$$\varphi_{\max} = \arccos\left[\left(\frac{2\nu_e^2 R_{\max}}{|1-\nu_e|}\right)^{\frac{1}{M}}\right]. \tag{19}$$

Next, for the same design, we consider *broadband*-modulated (~1 cycle) Gaussian pulsed excitation. Figure 3(A) and (B) show two numerically computed instantaneous field maps at time instants before the initial temporal boundary ($t < t_0$) and after the final one $t > t_M$, respectively. The BW wave is hardly visible on the scale of the plots and is better visualized in the saturated scale of Figure 3(C). Figure 3(D) shows instead a space-time field map, which better illustrates the evolution of the FW and BW wavefronts.

From a quantitative viewpoint, Figure 4(A) shows the (normalized) incident, FW, and BW waveforms at fixed positions, with the hardly visible BW component magnified in Figure 4(B). The corresponding (normalized) spectra are displayed in Figure 4(C), once again with the BW component magnified in Figure 4(D). As could be expected, with the exception of the edges of the Gaussian spectrum, the BW spectrum is in very good agreement with the theoretical design in Equation (17). To sum up, our proposed design enables a nearly reflectionless frequency conversion of a broadband pulse. It is also worth highlighting that, although the reflections are negligible, the FW transmitted field exhibits reduced amplitude; this is fully consistent with the general theory of transmission of electromagnetic waves at temporal boundaries [34].

As a second representative example, we consider the well-known Chebyshev-type design,

$$|R(\varphi)| = \frac{|1-\nu_e|}{2\nu_e^2}\left|\frac{T_M(\sec\varphi_{\max}\cos\varphi)}{T_M(\sec\varphi_{\max})}\right|, \tag{20}$$

with T_M denoting an Mth degree Chebyshev polynomial [46], which yields an *equi-ripple* response that maximizes the tradeoff between bandwidth and maximum reflection [40]. Also, in this case, the multiplicative constant is chosen so as to satisfy the self-consistency condition in Equation (10), whereas the band-edge $\varphi_{\max}$ is related to the maximum tolerable BW wave coefficient (magnitude) $R_{\max}$ via

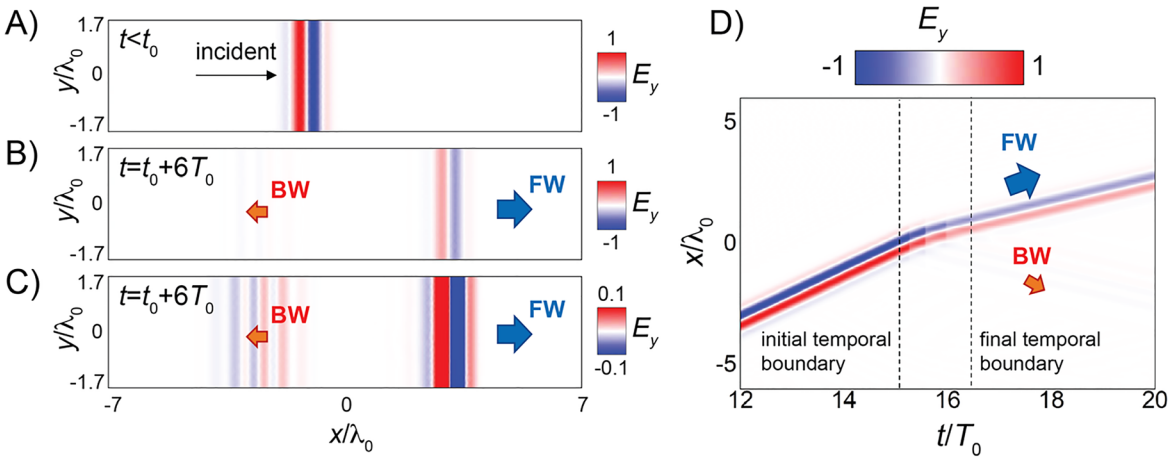

Figure 3: Parameters as in Figure 2 (binomial design), but broadband pulsed excitation.
(A), (B) Numerically computed instantaneous field maps (normalized electric field) at time instants before the initial temporal boundary and after the final one, respectively. (C) Same as panel (B), but with a saturated color scale, so as to better highlight the BW component. (D) Corresponding space-time map, with the vertical dashed lines indicating the initial and final temporal boundaries.

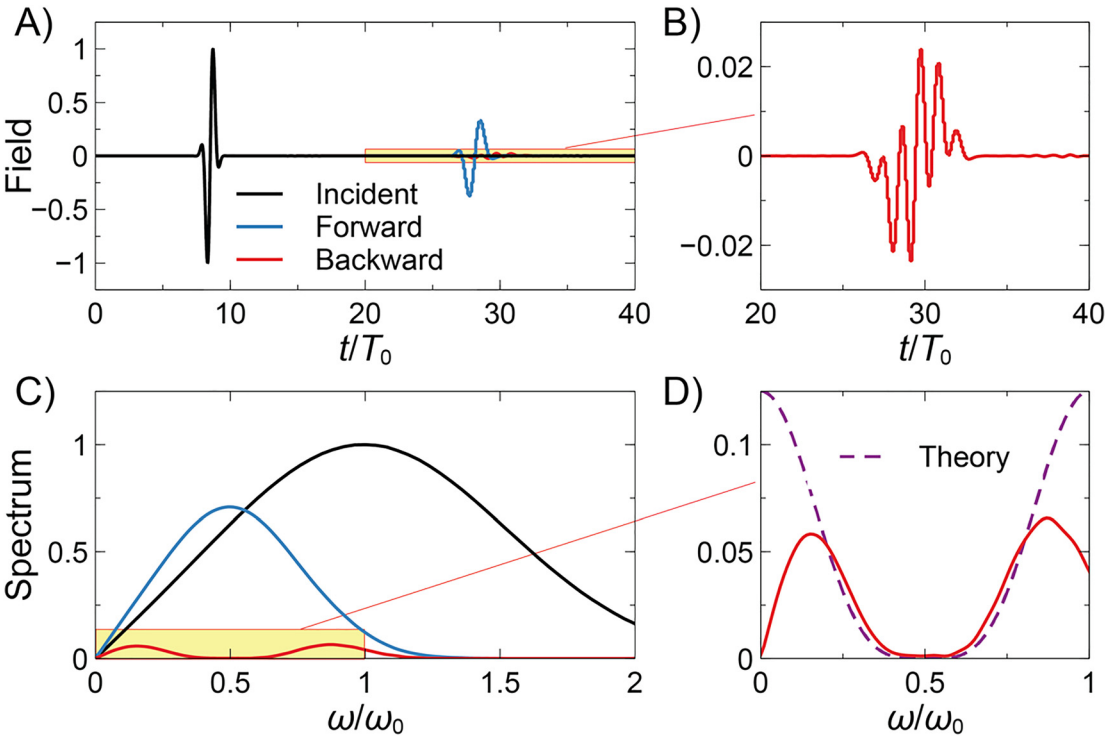

Figure 4: Parameters as in Figure 2 (binomial design), but broadband pulsed excitation.
(A) Numerically computed (normalized) incident, FW, and BW waveforms (black, blue, red curves, respectively) at fixed positions ($x = -6.7\lambda_0$ for the incident and BW waves, and $x = 6.7\lambda_0$ for the FW wave). (B) Magnified details of the BW waveform [yellow-shaded area in panel (A)]. (C) Corresponding (normalized) spectra (magnitude). (D) Magnified details of the BW spectrum [yellow-shaded area in panel (C)], compared with the theoretical prediction (purple-dashed curve).

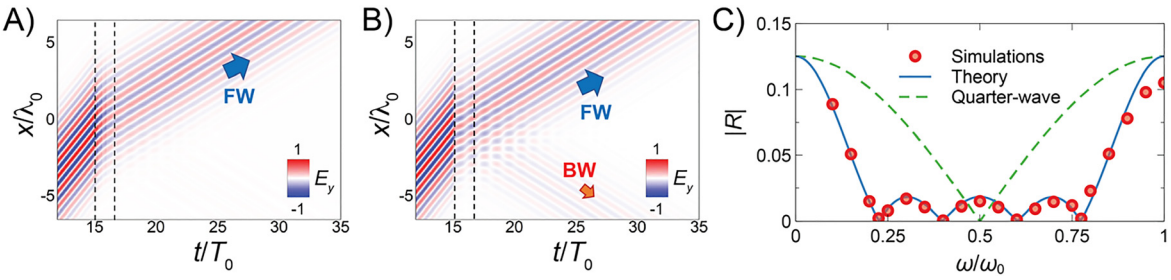

Figure 5: Chebyshev design: $n_i = 1$, $n_e = 2$, $M = 4$, $n_1 = 1.120$, $n_2 = 1.298$, $n_3 = 1.541$, $n_4 = 1.786$. $\delta_1 = 0.280T_0$, $\delta_2 = 0.324T_0$, $\delta_3 = 0.385T_0$, and $\delta_4 = 0.446T_0$.
(A), (B) Numerically computed space-time maps (normalized electric field) for narrowband modulated Gaussian pulses with center angular frequency ω_0 and $0.2\omega_0$, respectively. The vertical dashed lines indicate the initial ($t_0 = 15T_0$) and final ($t_M = 16.436T_0$) temporal boundaries. (C) Comparison between numerically computed (red circles) and theoretical (blue-solid curve) BW wave coefficient magnitude as a function of normalized angular frequency (in the final medium). Also shown (green-dashed curve), as a reference, is the response of the quarter-wave design ($M = 1$, $n_1 = 1.414$, and $\delta_1 = 0.354T_0$).

$$T_M(\sec\varphi_{\max}) = \frac{1}{R_{\max}}\left(\frac{|1-v_e|}{2v_e^2}\right), \tag{21}$$

which can be analytically inverted by resorting to the (hyperbolic) trigonometric expressions of the Chebyshev polynomials [46]. Once $\varphi_{\max}$ is known, the fractional bandwidth follows immediately from Equation (18).

For the Chebyshev design above, Figures 5–7 mirror the results shown in Figures 2–4, respectively, following the same layout and organization. The synthesized refractive indices and interval durations are given in the caption of Figure 5.

The same qualitative observations as for the binomial design essentially hold in this case too, with the obvious differences in the spectral BW response (see Figures 5(C) and 7(D)). Also, in this case, the agreement between numerical simulations and theoretical design is very good. We also observe that, although for different temporal multisteps the FW responses may differ even in the presence of very small reflections, in our example here the FW response is hardly distinguishable from the one in Figure 4 (binomial design).

3.2 Spatial discontinuity: toward broadband spatiotemporal impedance matching and frequency conversion

As a final example, we apply the temporal-impedance-transformer concept to a scenario featuring a spatial discontinuity between two stationary media. In this case, similar to what was proposed in Ref. [41] for the spatio-temporal quarter-wave antireflection temporal coating case, we introduce an intermediate spatial region where we apply the temporal modulation. More specifically, we assume an input region $x < -2.5\lambda_0$ with (stationary) refractive index n_i, an exterior region $x > \lambda_0$ with (stationary) refractive index n_e, and a central region $-2.5\lambda_0 < x < 2.5\lambda_0$ where we apply the temporal modulation according to the previously considered binomial and Chebyshev designs. The size of the central region as well as the initial ($t_0 = 15T_0$) and final ($t_M = 16.453T_0$ for the binomial, and $t_M = 16.436T_0$ for the Chebyshev case) temporal boundaries is chosen so as the temporal modulation is active while the incident pulse is propagating through this region.

For the same parameters and designs as in the previous examples (given in the captions of Figures 2 and 5) and broadband (~1 cycle) pulsed excitation, Figure 8 shows the numerically computed results in this scenario. Specifically, Figure 8(A)–(C) show two representative instantaneous field maps and the space-time field map pertaining to the binomial design, whereas Figure 8(D)–(F) show the corresponding results for the Chebyshev design. In both cases, we observe very weak BW (reflected) waves, which indicates that the temporal-impedance-transformer concept can be applied to spatial discontinuities as well via spatiotemporal modulations of the refractive index.

As a reference, Figure 8(G)–(I) show the results for the case of a *single-step* modulation, where the refractive index in the central region is changed abruptly from n_i to n_e at $t = t_0$ and then maintained constant. In this case, both spatial and temporal reflections are noticeably visible.

4 Conclusions

Via space-time duality, we have rigorously established a formal analogy between the reflectivity of a temporal multistep and the insertion loss of a conventional spatial

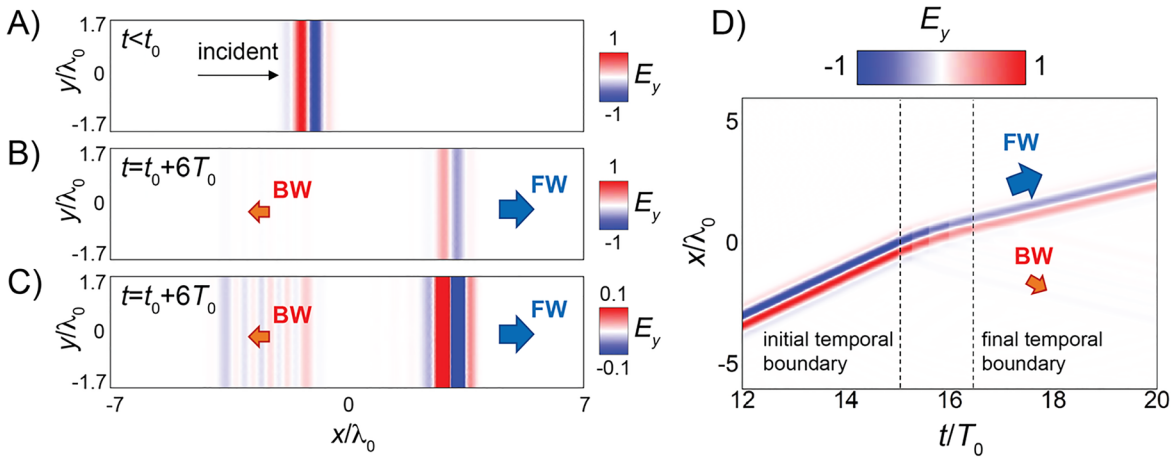

Figure 6: Parameters as in Figure 5 (Chebyshev design), but broadband pulsed excitation.
(A), (B) Numerically computed instantaneous field maps (normalized electric field) at time instants before the initial temporal boundary and after the final one, respectively. (C) Same as panel (B), but with a saturated color scale, so as to better highlight the BW component. (D) Corresponding space-time map, with the vertical dashed lines indicating the initial and final temporal boundaries.

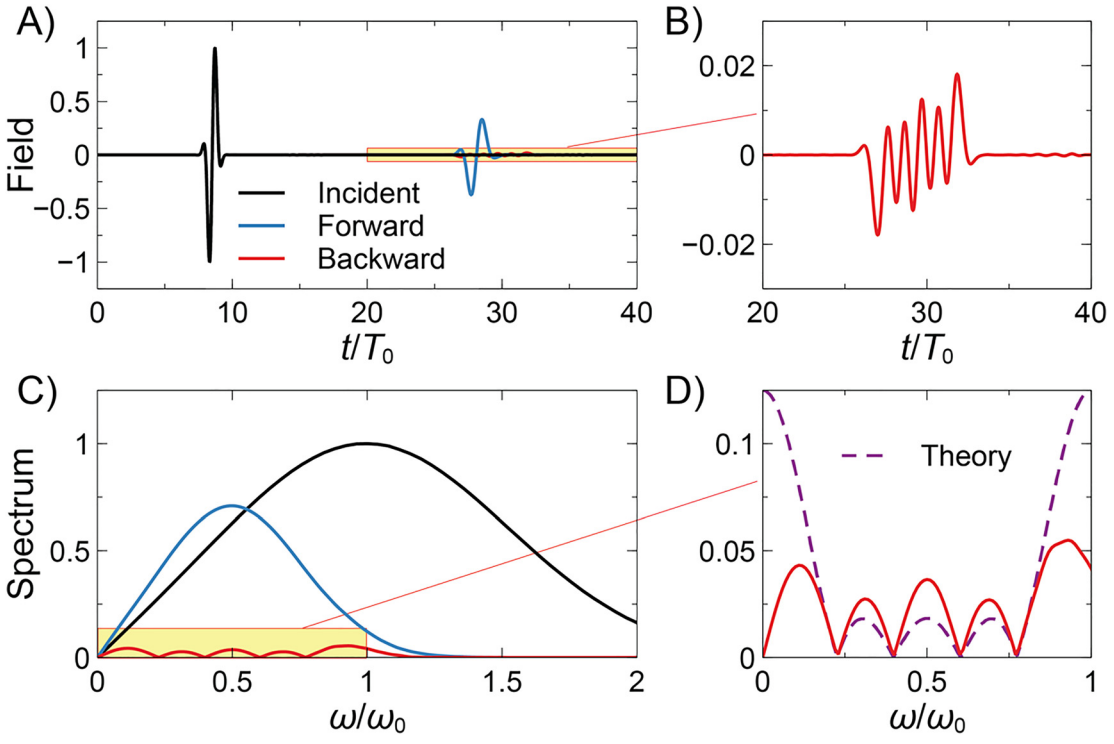

Figure 7: Parameters as in Figure 5 (Chebyshev design), but broadband pulsed excitation.
(A) Numerically computed (normalized) incident, FW, and BW waveforms (black, blue, red curves, respectively) at fixed positions. (B) Magnified details of the BW waveform [yellow-shaded area in panel (A)]. (C) Corresponding (normalized) spectra (magnitude). (D) Magnified details of the BW spectrum [yellow-shaded area in panel (C)], compared with the theoretical prediction (purple-dashed curve).

multilayer. This enables the systematic synthesis of the spectral response of temporal impedance transformers by resorting to well-established tools and approaches that are available in microwave engineering. As a proof of concept, we have carried out the synthesis of maximally flat (binomial) and equi-ripple (Chebyshev) responses, which extend and generalize the previously studied quarter-wave design [41]. Numerical validation

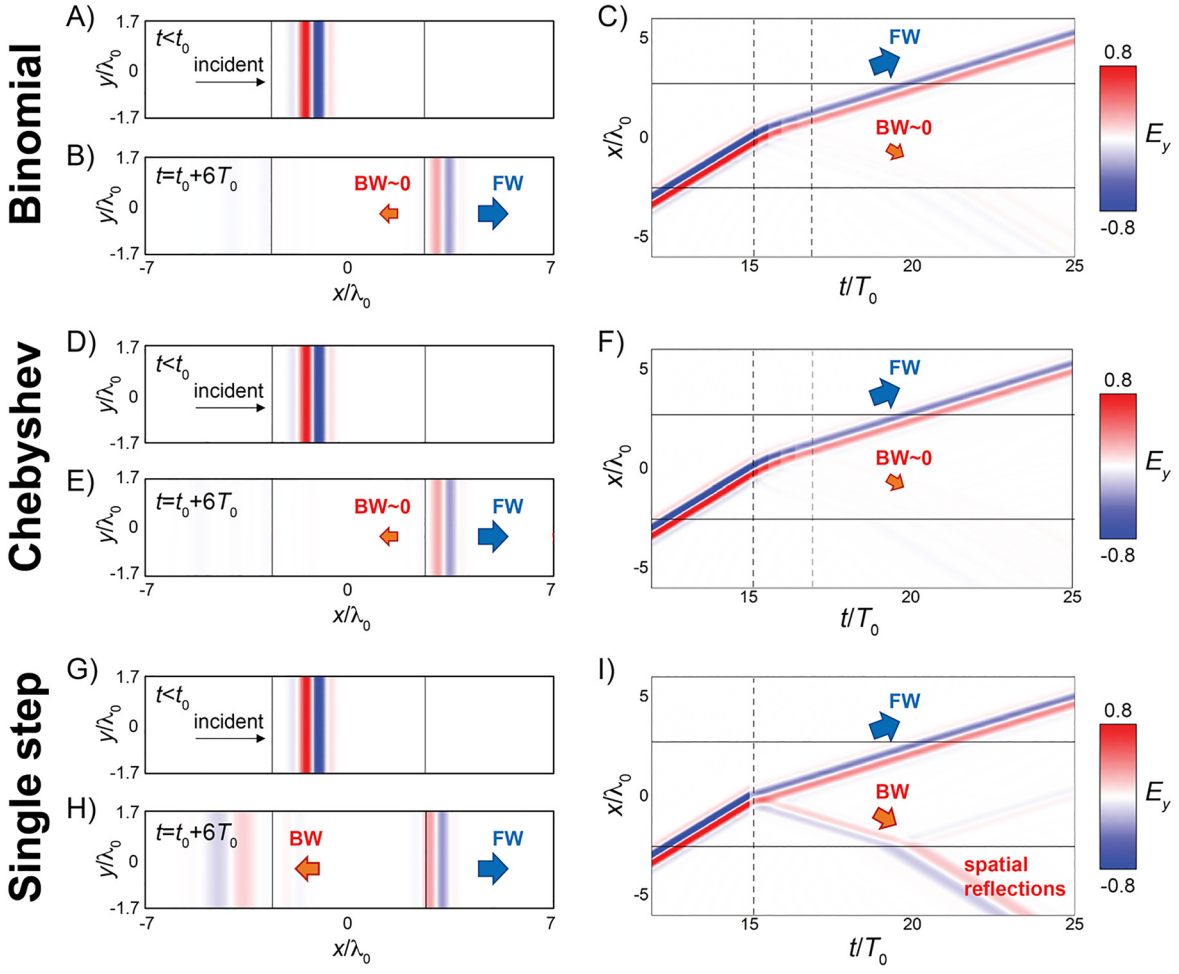

Figure 8: Spatial discontinuity between two stationary media with $n_i = 1$ and $n_e = 2$.
(A), (B) Numerically computed instantaneous field maps (normalized electric field) at two-time instants (before and after the initial and final temporal boundaries, respectively), by assuming a central region $-2.5\lambda_0 < x < 2.5\lambda_0$ where the refractive-index profile is modulated in time according to the binomial design (with parameters given in the caption of Figure 2). (C) Corresponding space-time map (normalized electric field). The continuous and dashed lines indicate the spatial and temporal boundaries, respectively. (D), (E), (F) As in panels (A), (B), (C), respectively, but for the Chebyshev design (with parameters given in the caption of Figure 5). (G), (H), (I) As in panels (A), (B), (C), respectively, but in for a single-step modulation, where the refractive index of the central region is abruptly switched from n_i to n_e at the temporal boundary $t_0 = 15T_0$, and then maintained constant.

(via finite-element simulations) has confirmed the possibility to attain nearly reflectionless, broadband frequency conversion, in excellent agreement with the theoretical predictions. Moreover, the approach can also be applied to bounded regions.

These outcomes shed further light on the formal analogies underpinning wave propagation in spatially modulated and time-varying media and set the stage for new exciting developments in the emerging field of space-time metastructures. To this aim, current and future studies are aimed at exploring the synthesis of broader class of spectral responses which may find a variety of interesting applications, including broadband absorbers [26], filters, photonic devices for frequency conversion, and analog signal processing [47].

Our proposed approach could potentially be experimentally implemented at microwaves using transmission lines loaded with reactive elements [48] and metasurfaces which can be actively controlled in time [49]. While our approach may be challenging to achieve at optical frequencies, we are hopeful that further technological developments may provide possibilities for enabling an experimental validation by using exotic scenarios such as, for instance, optical cavities [50].

5 Methods

5.1 Analytical modeling

For the spatial multilayers in Section 2.1 (see Figure 1(A)), our transfer-matrix formalism relies on effective voltages and currents related to the electric and magnetic (transverse) field components

$$V \leftrightarrow E_y, \quad I \leftrightarrow \frac{\eta}{n_i} H_z, \tag{22}$$

with $\eta = \sqrt{\mu_0/\epsilon_0}$ denoting the vacuum intrinsic impedance. Accordingly, the transfer matrix in Equation (1) relates the input and output values of these quantities for a generic layer, viz.,

$$\begin{bmatrix} V_m \\ I_m \end{bmatrix} = \underline{\underline{S}}_m \cdot \begin{bmatrix} V_{m-1} \\ I_{m-1} \end{bmatrix}, \quad m = 1, \ldots, M. \tag{23}$$

Assuming a unit-amplitude incident electric field, the total electric and magnetic fields outside the multilayer can be written as

$$E_y(x,t) = \exp(-i\omega t) \begin{cases} \exp(ikn_i x) + \rho \exp(-ikn_i x), & x < 0, \\ \tau \exp[ikn_e(x - x_M)], & x > x_M, \end{cases} \tag{24}$$

$$H_z(x,t) = \exp(-i\omega t) \begin{cases} \dfrac{n_i}{\eta}[\exp(ikn_i x) - \rho \exp(-ikn_i x)], & x < 0, \\ \dfrac{n_e \tau}{\eta} \exp[ikn_e(x - x_M)], & x > x_M, \end{cases} \tag{25}$$

with ρ and τ denoting the conventional reflection and transmission coefficients, respectively. From Equations (24) and (25), we can straightforwardly obtain the effective voltage and current at the input interface ($x = 0$) as $V_0 = 1 + \rho$, $I_0 = 1 - \rho$, and at the output interface ($x = x_M$) as $V_M = \tau$, $I_M = \nu_e \tau$, which are connected by multilayer the transfer matrix in Equation (2),

$$\begin{bmatrix} V_M \\ I_M \end{bmatrix} = \begin{bmatrix} s_{11} & is_{12} \\ is_{21} & s_{22} \end{bmatrix} \cdot \begin{bmatrix} V_0 \\ I_0 \end{bmatrix}. \tag{26}$$

By solving the above linear system with respect to ρ and τ, we obtain the expression in Equation (3) and

$$\tau = \frac{2}{s_{22} - is_{21} + \nu_e(s_{11} - is_{12})}. \tag{27}$$

For the temporal multisteps in Section 2.2 (see Figure 1(B)), our transfer-matrix model relies instead on effective voltages and currents that are related to the (normalized) magnetic and electric induction, respectively,

$$V \leftrightarrow \frac{cB_z}{n_i}, \quad I \leftrightarrow -\frac{D_y}{n_i^2 \epsilon_0}, \tag{28}$$

where

$$B_z = \mu_0 H_z, \quad D_y = \epsilon_0 n^2 E_y. \tag{29}$$

We highlight that the specific expressions and normalizations in Equation (28) are instrumental to obtain the transfer matrix in Equation (4), which is formally analogous to that for the spatial case in Equation (1); this is crucial to reveal the space-time duality. Once again, assuming a unit-amplitude electric field, the total electric and magnetic fields before the first temporal boundary and after the final one can be written as

$$E_y(x,t) = \exp(ikn_i x) \begin{cases} \exp[-i\omega(t - t_0)], & t < t_0, \\ T \exp\left[-\dfrac{i\omega}{\nu_e}(t - t_M)\right] + R \exp\left[\dfrac{i\omega}{\nu_e}(t - t_M)\right], & t > t_M, \end{cases} \tag{30}$$

$$H_z(x,t) = \exp(ikn_i x) \begin{cases} \dfrac{n_i}{\eta} \exp[-i\omega(t - t_0)], & t < t_0, \\ \dfrac{n_e}{\eta} \left\{ T \exp\left[-\dfrac{i\omega}{\nu_e}(t - t_M)\right] - R \exp\left[\dfrac{i\omega}{\nu_e}(t - t_M)\right] \right\}, & t > t_M, \end{cases} \tag{31}$$

with R and T denoting the BW and FW wave coefficients, respectively [34]. By comparison with the spatial case in Equations (24) and (25), we note the conservation of the wavenumber (instead of frequency), and the different role played by the reflection coefficient, which does not appear before the first temporal boundary in view of causality. By proceeding as in the spatial case, we can write the effective voltage and current at the initial temporal boundary ($t = t_0$) as $V_0 = 1$, $I_0 = -1$, and those at the final one ($t = t_M$) as $V_M = \nu_e(T - R)$, $I_M = -\nu_e^2(T + R)$, and we can solve the resulting linear system, analogous to that in Equation (26), in terms of R and T. This yields the expression in Equation (5) and

$$T = \frac{s_{22} + is_{21}}{2\nu_e^2} + \frac{s_{11} + is_{12}}{2\nu_e}. \tag{32}$$

5.2 Riblet-type synthesis

For completeness, we summarize the salient steps of the synthesis procedure, referring the reader to Ref. [43] for its theoretical foundations and more details. In essence, starting from the insertion-loss function in Equation (11), the *complex-valued* reflection coefficient is reconstructed as

$$\rho(\theta) = \frac{\alpha Q_M(\cos\theta)}{\cos^M\theta + \cos^{M-2}\theta + \cdots + i\sin\theta(\cos^{M-1}\theta + \cos^{M-3} + \cdots)}, \tag{33}$$

where the multiplicative constant α must be chosen so as to satisfy the self-consistency relationship in Equation (9), and the denominator has been constructed by retaining only the poles in the upper half of the complex ω-plane [i.e., $\mathrm{Im}(\omega) \geq 0$], so as to ensure unconditional stability.

From Equation (33), the normalized impedance at the input interface $x = 0$ can be derived as

$$\overline{Z}_0 = \frac{V_0}{I_0} = \frac{1 + \rho(\theta)}{1 - \rho(\theta)}. \tag{34}$$

Then, recalling the transport formula of the normalized impedance through a layer,

$$\overline{Z}_m = \frac{V_m}{I_m} = \frac{\cos\theta \overline{Z}_{m-1} + \dfrac{i\sin\theta}{\nu_m}}{\cos\theta + i\nu_m \sin\theta \overline{Z}_{m-1}}, \tag{35}$$

it is possible to iteratively solve for the unknown normalized refractive indices ν_m, $m = 1, \ldots, M$. Specifically, starting from the first layer ($m = 1$), we obtain

$$\overline{Z}_1 = \frac{\cos\theta\overline{Z}_0 + \dfrac{i\sin\theta}{\nu_1}}{\cos\theta + i\nu_1\sin\theta\overline{Z}_0}, \tag{36}$$

where $\overline{Z}_0$ is given in Equation (34), and ν_1 can be computed by enforcing that the degree of the numerator and denominator is $M-1$. By proceeding iteratively, for $m = 2, 3, \ldots, M$, and enforcing that at each step the degree is lowered by one, we can compute all remaining values of ν_m.

5.3 Numerical modeling

All the numerical simulations in this study are carried out by means of the finite-element-based commercial software COMSOL Multiphysics® [51]. Specifically, we utilize the time-domain solver, and consider a two-dimensional computational domain truncated by top and bottom perfectly electric conducting walls and left and right scattering boundary conditions to excite the incident field and prevent reflections, respectively. The computational domain is discretized via a triangular mesh with size ranging from $10^{-4}\lambda_0$ to $0.15\lambda_0$.

For the narrowband excitation in Figures 2 and 5, a number of separate simulations are carried out, with Gaussian pulses featuring different modulation frequencies (ω_{mod} ranging from $0.2\omega_0$ to ω_0) and standard deviations $2T_{\mathrm{mod}} = 4\pi/\omega_{\mathrm{mod}}$; these pulses include approximately 12 cycles.

For the broadband excitation in Figures 3, 4, 6–8 we consider instead a modulated Gaussian pulse with $\omega_{\mathrm{mod}} = \omega_0$ and standard deviation $0.3T_{\mathrm{mod}} = 0.6\pi/\omega_0$, which includes approximately one cycle. The spectra in Figures 4(C) and 7(C) are obtained via fast Fourier transform of the corresponding waveforms, implemented via the `fft` routine available in Matlab® [52].

The abrupt refractive index changes are implemented via rectangular analytical functions with smooth transitions. The duration of the transitions is much smaller than the modulation period ($\sim 0.01T_{\mathrm{mod}}$) in order to induce the temporal boundary, and two continuous derivatives are applied to the smooth transitions to ensure the convergence of the simulations.

Author contributions: All the authors have accepted responsibility for the entire content of this submitted manuscript and approved submission.

Research funding: G.C. and V.G. acknowledge partial support from the University of Sannio via the FRA 2019 Program. V.P-P acknowledges support from Newcastle University (Newcastle University Research Fellowship). N.E. acknowledges partial support from the Simons Foundation on Symmetry-Driven Extreme Wave Phenomena, Award Number: 733684.

Conflict of interest statement: The authors declare no conflicts of interest regarding this article.

References

[1] F. R. Morgenthaler, "Velocity modulation of electromagnetic waves," *IRE Trans. Microw. Theor. Tech.*, vol. 6, no. 2, pp. 167–172, 1958.

[2] A. A. Oliner and A. Hessel, "Wave propagation in a medium with a progressive sinusoidal disturbance," *IRE Trans. Microw. Theor. Tech.*, vol. 9, no. 4, pp. 337–343, 1961.

[3] R. Fante, "Transmission of electromagnetic waves into time-varying media," *IEEE Trans. Antenn. Propag.*, vol. 19, no. 3, pp. 417–424, 1971.

[4] A. M. Shaltout, K. G. Lagoudakis, J. van de Groep, et al., "Spatiotemporal light control with frequency-gradient metasurfaces," *Science*, vol. 365, no. 6451, pp. 374–377, 2019.

[5] C. Caloz and Z. Deck-Léger, "Spacetime metamaterials—Part I: general concepts," *IEEE Trans. Antenn. Propag.*, vol. 68, no. 3, pp. 1569–1582, 2020.

[6] C. Caloz and Z. Deck-Léger, "Spacetime metamaterials—Part II: theory and applications," *IEEE Trans. Antenn. Propag.*, vol. 68, no. 3, pp. 1583–1598, 2020.

[7] N. Engheta, "Metamaterials with high degrees of freedom: space, time, and more," *Nanophotonics*, vol. 10, no. 1, pp. 639–642, 2021.

[8] K. Fang, Z. Yu, and S. Fan, "Realizing effective magnetic field for photons by controlling the phase of dynamic modulation," *Nat. Photonics*, vol. 6, no. 11, pp. 782–787, 2012.

[9] R. Fleury, D. L. Sounas, C. F. Sieck, M. R. Haberman, and A. Alù, "Sound isolation and giant linear nonreciprocity in a compact acoustic circulator," *Science*, vol. 343, no. 6170, pp. 516–519, 2014.

[10] Y. Hadad, D. L. Sounas, and A. Alù, "Space-time gradient metasurfaces," *Phys. Rev. B*, vol. 92, no. 10, p. 100304, 2015.

[11] A. Shaltout, A. V. Kildishev, and V. M. Shalaev, "Time-varying metasurfaces and Lorentz non-reciprocity," *Opt. Mater. Express*, vol. 5, no. 11, pp. 2459–2467, 2015.

[12] Y. Hadad, J. C. Soric, and A. Alù, "Breaking temporal symmetries for emission and absorption.," *Proc. Natl. Acad. Sci. U.S.A.*, vol. 113, no. 13, pp. 3471–3475, 2016.

[13] L. Zhang, X. Q. Chen, R. W. Shao, et al., "Breaking reciprocity with space-time-coding digital metasurfaces," *Adv. Mater.*, vol. 31, no. 41, p. 1904069, 2019.

[14] X. Guo, Y. Ding, Y. Duan, and X. Ni, "Nonreciprocal metasurface with space–time phase modulation," *Light Sci. Appl.*, vol. 8, p. 123, 2019.

[15] V. Bacot, M. Labousse, A. Eddi, M. Fink, and E. Fort, "Time reversal and holography with spacetime transformations," *Nat. Phys.*, vol. 12, no. 10, pp. 972–977, 2016.

[16] S. M. Mirmosa, A. G. Ptitcyn, V. S. Asadchy, and S. A. Tretyakov, "Time-varying reactive elements for extreme accumulation of electromagnetic energy," *Phys. Rev. Appl.*, vol. 11, no. 1, p. 014024, 2019.

[17] D. Ramaccia, D. L. Sounas, A. Alù, A. Toscano, and F. Bilotti, "Phase-induced frequency conversion and Doppler effect with time-modulated metasurfaces," *IEEE Trans. Antenn. Propag.*, vol. 68, no. 3, pp. 1607–1617, 2020.

[18] A. Akbarzadeh, N. Chamanara, and C. Caloz, "Inverse prism based on temporal discontinuity and spatial dispersion," *Opt. Lett.*, vol. 43, no. 14, pp. 3297–3300, 2018.

[19] P. A. Huidobro, E. Galiffi, S. Guenneau, R. V. Craster, and J. B. Pendry, "Fresnel drag in space–time-modulated metamaterials," *Proc. Natl. Acad. Sci. U.S.A.*, vol. 116, no. 50, pp. 24943–24948, 2019.

[20] L. Zhang, X. Q. Chen, S. Liu, et al., "Space-time-coding digital metasurfaces," *Nat. Commun.*, vol. 9, p. 4334, 2018.

[21] Z. Wu, C. Scarborough, and A. Grbic, "Space-time-modulated metasurfaces with spatial discretization: free-space N-path systems," *Phys. Rev. Appl.*, vol. 14, no. 6, p. 064060, 2020.
[22] G. Castaldi, L. Zhang, M. Moccia, et al., "Joint multi-frequency beam shaping and steering via space–time-coding digital metasurfaces," *Adv. Funct. Mater.*, vol. 31, no. 6, p. 2007620, 2021.
[23] E. Galiffi, Y.-T. Wang, Z. Lim, J. B. Pendry, A. Alù, and P. A. Huidobro, "Wood anomalies and surface-wave excitation with a time grating," *Phys. Rev. Lett.*, vol. 125, no. 12, p. 127403, 2020.
[24] S. Taravati and G. V. Eleftheriades, "Generalized space-time-periodic diffraction gratings: theory and applications," *Phys. Rev. Appl.*, vol. 12, no. 2, p. 024026, 2019.
[25] A. Shlivinski and Y. Hadad, "Beyond the Bode-Fano bound: wideband impedance matching for short pulses using temporal switching of transmission-line parameters," *Phys. Rev. Lett.*, vol. 121, no. 20, p. 204301, 2018.
[26] H. Li, A. Mekawy, and A. Alù, "Beyond Chu's limit with Floquet impedance matching," *Phys. Rev. Lett.*, vol. 123, no. 16, p. 164102, 2019.
[27] H. Li and A. Alù, "Temporal switching to extend the bandwidth of thin absorbers," *Optica*, vol. 8, no. 1, pp. 24–29, 2021.
[28] H. Barati Sedeh, M. M. Salary, and H. Mosallaei, "Time-varying optical vortices enabled by time-modulated metasurfaces," *Nanophotonics*, vol. 9, no. 9, pp. 2957–2976, 2020.
[29] V. Pacheco-Peña and N. Engheta, "Temporal aiming," *Light Sci. Appl.*, vol. 9, p. 129, 2020.
[30] V. Pacheco-Peña and N. Engheta, "Temporal Brewster angle," *arXiv:2102.13305 [physics]*, 2021, Submitted for publication.
[31] V. Pacheco-Peña and N. Engheta, "Spatiotemporal isotropic-to-anisotropic meta-atoms," *arXiv:2106.12471 [physics]*, 2021, Submitted for publication.
[32] H. Li, H. Moussa, D. Sounas, and A. Alù, "Parity-time symmetry based on time modulation," *Phys. Rev. Appl.*, vol. 14, no. 3, p. 031002, 2020.
[33] H. Kazemi, M. Y. Nada, T. Mealy, A. F. Abdelshafy, and F. Capolino, "Exceptional points of degeneracy induced by linear time-periodic variation," *Phys. Rev. Appl.*, vol. 11, no. 1, p. 014007, 2019.
[34] Y. Xiao, D. N. Maywar, and G. P. Agrawal, "Reflection and transmission of electromagnetic waves at a temporal boundary," *Opt. Lett.*, vol. 39, no. 3, pp. 574–577, 2014.
[35] D. Ramaccia, A. Toscano, and F. Bilotti, "Light propagation through metamaterial temporal slabs: reflection, refraction, and special cases," *Opt. Lett.*, vol. 45, no. 20, pp. 5836–5839, 2020.
[36] J. Li, X. Zhu, C. Shen, X. Peng, and S. A. Cummer, "Transfer matrix method for the analysis of space-time-modulated media and systems," *Phys. Rev. B*, vol. 100, no. 14, p. 144311, 2019.
[37] V. Pacheco-Peña and N. Engheta, "Effective medium concept in temporal metamaterials," *Nanophotonics*, vol. 9, no. 2, pp. 379–391, 2020.
[38] D. Torrent, "Strong spatial dispersion in time-modulated dielectric media," *Phys. Rev. B*, vol. 102, no. 21, p. 214202, 2020.
[39] P. Yeh, *Optical Waves in Layered Media*, New York, NY, Wiley, 2005.
[40] R. E. Collin, *Foundations for Microwave Engineering*, Hoboken, NJ, Wiley-IEEE Press, 2001.
[41] V. Pacheco-Peña and N. Engheta, "Antireflection temporal coatings," *Optica*, vol. 7, no. 4, pp. 323–331, 2020.
[42] D. Ramaccia, A. Alù, A. Toscano, and F. Bilotti, "Temporal multilayer structures for designing higher-order transfer functions using time-varying metamaterials," *Appl. Phys. Lett.*, vol. 118, no. 10, p. 101901, 2021.
[43] H. J. Riblet, "General synthesis of quarter-wave impedance transformers," *IEEE Trans. Microw. Theor. Tech.*, vol. 5, no. 1, pp. 36–43, 1957.
[44] D. M. Solís and N. Engheta, "Functional analysis of the polarization response in linear time-varying media: A generalization of the Kramers-Kronig relations," *Phys. Rev. B*, vol. 103, no. 14, p. 144303, 2021.
[45] R. E. Collin, "Theory and design of wide-band multisection quarter-wave transformers," *Proc. IRE*, vol. 43, no. 2, pp. 179–185, 1955.
[46] M. Abramowitz and I. A. Stegun, *Handbook of Mathematical Function: With Formulas Graphs, and Mathematical Tables*, New York, NY, Dover, 1965.
[47] A. Silva, F. Monticone, G. Castaldi, V. Galdi, A. Alù, and N. Engheta, "Performing mathematical operations with metamaterials," *Science*, vol. 343, no. 6167, pp. 160–163, 2014.
[48] A. Kord, M. Tymchenko, D. L. Sounas, H. Krishnaswamy, and A. Alù, "CMOS integrated magnetless circulators based on spatiotemporal modulation angular-momentum biasing," *IEEE Trans. Microw. Theor. Tech.*, vol. 67, no. 7, pp. 2649–2662, 2019.
[49] K. Lee, J. Son, J. Park, et al., "Linear frequency conversion via sudden merging of meta-atoms in time-variant metasurfaces," *Nat. Photonics*, vol. 12, no. 12, pp. 765–773, 2018.
[50] S. F. Preble, Q. Xu, and M. Lipson, "Changing the colour of light in a silicon resonator," *Nat. Photonics*, vol. 1, no. 5, pp. 293–296, 2007.
[51] COMSOL AB, *COMSOL Multiphysics® v. 5.1*, Stockholm, Sweden, COMSOL AB, 2015.
[52] MATLAB, *9.7.0.1190202 (R2019b)*, Natick, Massachusetts, The MathWorks Inc., 2018.